Available online at www.sciencedirect.com
ScienceDirect
Trans. Nonferrous Met. Soc. China 32(2022) 1926−1934
Transactions of Nonferrous Metals Society of China
www.tnmsc.cn

Effects of shape and size of second phase on mechanical properties of sintered Mo−Y_2O_3 alloys

Zhuang-zhi WU[1,2], Na ZHAO[1], Yao LU[1], Hai-lang LIU[3], Bo-hua DUAN[1,2], Xin-li LIU[1,2], De-zhi WANG[1,2]

1. School of Materials Science and Engineering, Central South University, Changsha 410083, China;
2. Key Laboratory of Non-ferrous Materials Science and Engineering, Ministry of Education, Central South University, Changsha 410083, China;
3. Guangxi Key Laboratory of Manufacturing Systems and Advanced Manufacturing Technology, Guilin University of Electronic Technology, Guilin 541004, China

Received 27 July 2021; accepted 17 November 2021

Abstract: The morphology and size of second phase greatly influence the strengthening effect on oxidation dispersion strengthened Mo alloys. In this work, a novel nanostructuring strategy is adopted to modify the second phase of Y_2O_3, and the corresponding effects of particle shape and size on mechanical properties of sintered Mo−Y_2O_3 alloys were investigated. It is found that spherical particles with sizes below 200 nm are preferred due to the dominant intragranular distribution of second phases associated with better strengthening effect originating from dislocation pinning. With smaller particle size of Y_2O_3 nanospheres (105 nm), the tensile strength of corresponding Mo alloy is enhanced by about 43.8%, much higher than that (8.3%) reinforced by second phase nanospheres with larger particle size (322 nm). Meanwhile, with similar particle size (around 100 nm), the spherical shape exhibits better strengthening effect than the one reinforced by one-dimensional rod-like second phase.

Key words: Mo-based alloys; second phase; yttrium oxide; mechanical properties; dispersion strengthening

1 Introduction

Molybdenum (Mo) alloys with ultra-high melting point, low expansion coefficient, excellent thermal and electrical conductivities have shown wide applications in the fields of petroleum, lighting, aerospace, metallurgy, and so on [1−4]. However, the low high-temperature strength, low recrystallization temperature and high ductile-to-brittle transition temperature still restrict further applications of Mo alloys. Many researchers have put forward the scheme of adding other elements or rare earth oxides into Mo to overcome the above disadvantages [5−9]. ZrO_2 makes the Mo−ZrO_2 alloy have higher strength and elongation at room temperature than pure molybdenum [5]. The addition of Al_2O_3 can refine the grain size and increase the micro-hardness of Mo alloy [6,7]. ZHANG et al [8] doped Mo alloy with La_2O_3, which improved toughness and decreased the DBTT (ductile-to-brittle transition temperature) of Mo alloy. WU et al [9] synthesized Mo−La_2O_3 powder by self-reduction strategy, which exhibited excellent sintering performance with greatly relative density and hardness.

Among rare earth metals, yttrium (Y) presents strong oxidation ability, so it can purify the grain boundary (GB) by adsorbing and capturing impurities such as C, N and O in Mo alloys [10]. In addition, Y_2O_3 shows close melting point with molybdenum, stable chemical properties, excellent heat resistance and corrosion resistance, and can greatly improve the recrystallization temperature,

---

Corresponding author: Xin-li LIU, E-mail: liuxinli@csu.edu.cn
DOI: 10.1016/S1003-6326(22)65919-3

reduce the ductile-to-brittle transition temperature, refine grain size, and improve the strength and hardness of Mo alloys [11,12]. Generally, the strengthening mechanisms for rare earth oxides as second phase particles can be ascribed to reducing the segregation of impurity elements (including O, C and N) at GBs to enhance the bonding ability and increasing migration resistance of dislocations to improve the strength of Mo alloys [3,13−18]. Great efforts have been devoted to developing high-performance Mo−Y_2O_3 alloys, including doping other rare metal oxides, and using the spark plasma sintering technique [16−18]. However, there are few reports on the intrinsic regulations of Y_2O_3, in which the size and morphology heavily influence the mechanical performances of Mo−Y_2O_3 alloys.

In this work, we proposed a nanostructuring strategy over the Y_2O_3 particles to improve the mechanical performances of Mo alloy, in which the size and shape of second phase were well modulated, and the strengthening effects of the second phase were also be clarified systematically.

2 Experimental

2.1 Synthesis of powders

Typically, urea (CON_2H_4, 30 g, Aladdin Reagents Company) and $Y(NO_3)_3·6H_2O$ (4.3 g, Shanghai Crystal Bio-chemical Technology Company) were mixed by deionized water with a concentration ratio of 30:1, and then 5 mL CTAB solution (cetyl trimethyl ammonium bromide, 3 g/L, Aladdin Reagents Company) was slowly added into the mixture, and then the mixture was kept at 90 °C for 1 h. The addition of CTAB is to control the resulting Y_2O_3 morphology into a spherical shape [19]. After being washed with deionized water and alcohol thrice, the precipitate was collected and dried for 12 h at 80 °C and then calcined in vacuum at 800 °C for 4 h. Y_2O_3 nanospheres with small size of 105 nm were obtained and named as 105-SY_2O_3. When the hydrothermal time was increased up to 12 h, Y_2O_3 nanospheres with large size of 322 nm can be gained and named as 322-SY_2O_3.

To prepare Y_2O_3 nanorods, $Y(NO_3)_3·6H_2O$ (5.8 g) and $NH_3·H_2O$ (adjusting pH value to 9) were mixed in 20 mL water by magnetically stirring for 0.5 h, and then the mixture reacted at 120 °C for 6 h. The precipitate was collected after being centrifuged and washed thrice with alcohol and water, respectively and then annealed at 800 °C for 4 h. Consequently, Y_2O_3 nanorods were obtained and denoted as RY_2O_3.

Mo powders were prepared by a traditional two-step hydrogen reduction method, in which $(NH_4)_6Mo_7O_{24}·4H_2O$ (purity of 99.9%, Jinduicheng Molybdenum Industry Group, China) was firstly calcined at 400 °C for 60 min to obtain MoO_3, then reduced by H_2 at 550 °C for 60 min to obtain MoO_2. Finally, MoO_2 was reduced at 900 °C for 60 min to produce pure Mo powders.

2.2 Sintering

The prepared Mo and 1 wt.% of various Y_2O_3 powders (322-SY_2O_3, RY_2O_3 and 105-SY_2O_3) were mixed uniformly with a planetary mixer at a ball-to-material mass ratio of 20:1 for 14 h, and then suppressed in a mold (40 mm in diameter) under 200 MPa for 60 s. The sintering was conducted in a high temperature hydrogen box furnace (KSL−1700X, Hefei Kejing Company, China). The specific sintering process is shown in Fig. 1. Finally, various sintered billets were collected and denoted as PMo, 322-SY_2O_3−Mo, RY_2O_3−Mo, and 105-SY_2O_3−Mo, respectively.

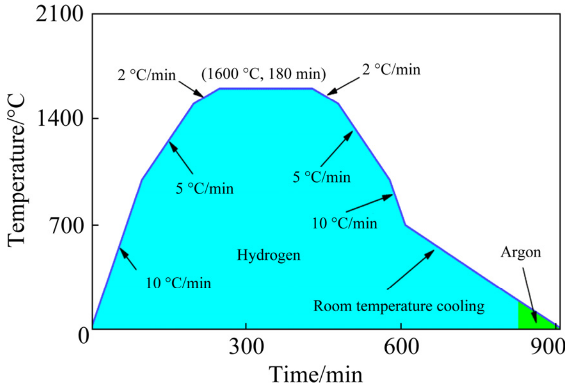

Fig. 1 Schematic diagram of sintering process

2.3 Characterization

The as-synthesized samples were characterized by X-ray diffractometer (Rigaku D/Max 2500), field emission scanning electron microscope equipped with EDS (FESEM, SIRION200), and field emission transmission electron microscope (TEM, Tecnai G^2 20), respectively. The density was measured using a densitometer (DE−120 M). The hardness was obtained by a microhardness tester

(HVS−1000) with 300 g for 10 s. The mechanical performance was evaluated using universal testing machine (Instron 8802) at room temperature with loading rate of 1 mm/min. The shape and dimension for tensile and compressive tests are those in Ref. [20].

3 Results

3.1 XRD patterns and microstructures of prepared Mo and Y_2O_3 powders

The XRD patterns of the obtained powders are shown in Fig. 2. Obviously, the prepared Mo powder is well indexed to pure Mo (PDF No. 42-1120) and highly crystallized (Fig. 2(a)). The XRD patterns of the synthesized Y_2O_3 are presented in Fig. 2(b), and all the characteristic peaks correspond to pure Y_2O_3 (PDF No. 83-0927).

The prepared Mo powders are polygonal with obvious interface, and present relatively uniform particle size distribution with an average size of 500 nm, as shown in Fig. 3(a). Figures 3(b−d) display SEM images of the obtained Y_2O_3 particles.

It can be seen that the 105-SY_2O_3 particles are relatively uniform in size and perfectly spherical with an average size of 105 nm (Fig. 3(b)). With

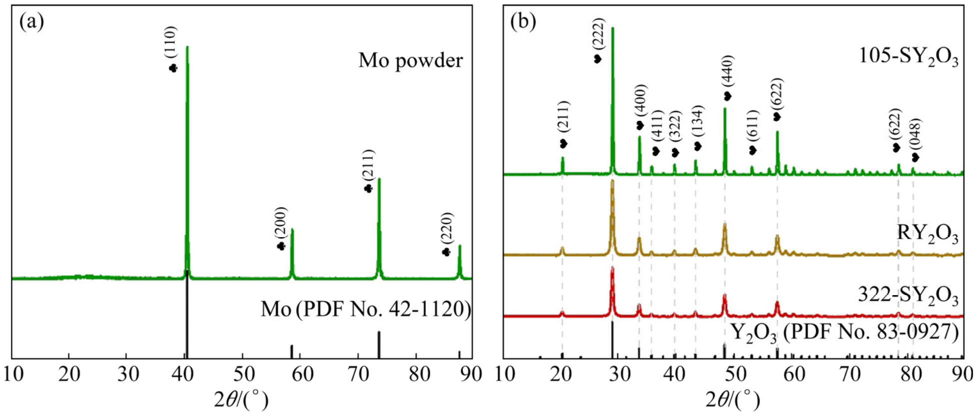

Fig. 2 XRD patterns of synthesized Mo (a) and various Y_2O_3 powders (b)

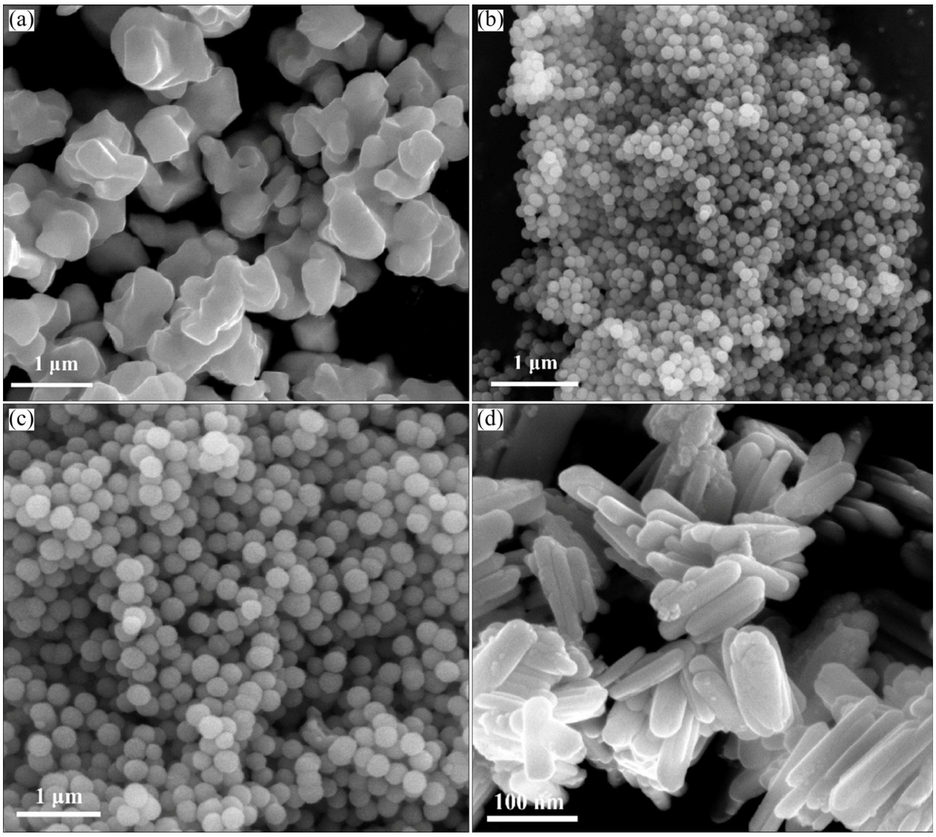

Fig. 3 SEM images of prepared powders: (a) Mo; (b) 105-SY_2O_3; (c) 322-SY_2O_3; (d) RY_2O_3

elongated reaction duration, larger spherical particles can be collected with an average size of 322 nm, which are named as 322-SY_2O_3, as revealed in Fig. 3(c). Besides, the SEM image of RY_2O_3 demonstrates the one-dimensional structures with an average length of 115 nm, as presented in Fig. 3(d).

3.2 Microstructures and properties of sintered billets

After being sintered at 1600 °C for 3 h, compact billets can be obtained, and the corresponding SEM images are presented in Fig. 4. It can be found that PMo has more pores than the Mo−Y_2O_3 alloys, indicating smaller density. Moreover, the average grain size of the PMo is much larger than those of Mo−Y_2O_3 alloys, demonstrating that the addition of Y_2O_3 can inhibit the migration of GBs, effectively refining the grains and improving the shrinkage rate and relative density [3].

The shrinkage rate and relative density of the synthesized PMo and various Mo−Y_2O_3 alloys are compared in Fig. 5(a). It can be seen that the shrinkage rates of PMo, 322-SY_2O_3−Mo, RY_2O_3−Mo, and 105-SY_2O_3−Mo alloys are 0.19%, 0.21%, 0.23%, and 0.25%, respectively. All the samples show satisfied relative density over 95%, and the addition of Y_2O_3 further promotes the densification, leading to larger relative density. And the 105-SY_2O_3−Mo presents the largest relative density of 97.55%. The grain size and hardness are compared in Fig. 5(b), in which the grain size of PMo is about 10.6 μm, while those of 322-SY_2O_3−Mo, RY_2O_3−Mo, and 105-SY_2O_3−Mo alloys are 8.5, 7.1, and 6.1 μm, respectively, indicating that the 105-SY_2O_3 exhibits the best grain refinement effect. Evidently, the presence of Y_2O_3 can effectively reduce the particle size of Mo originating from the migration resistance of GBs, which is consistent with the analysis of Fig. 4. Furthermore, the hardness of Mo alloys is also enlarged due to the

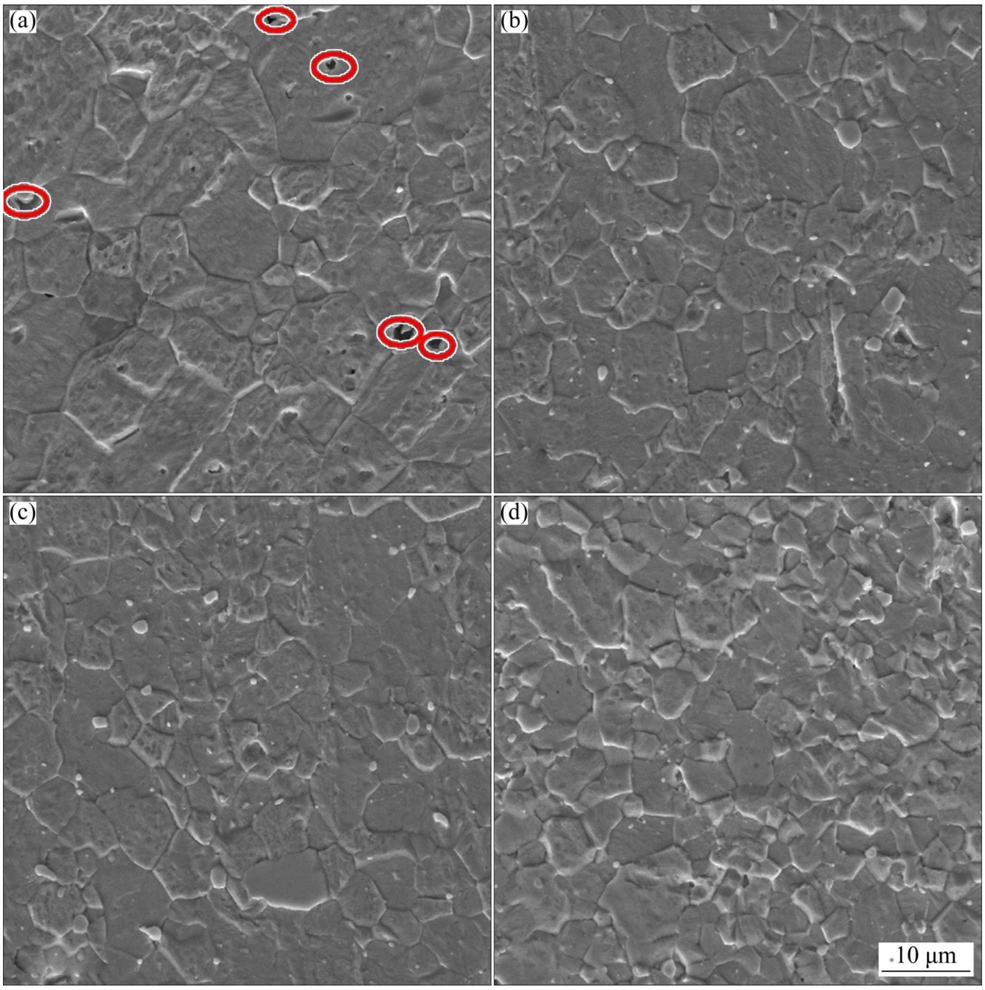

Fig. 4 SEM images of PMo (a), 322-SY_2O_3−Mo (b), RY_2O_3−Mo (c) and 105-SY_2O_3−Mo (d)

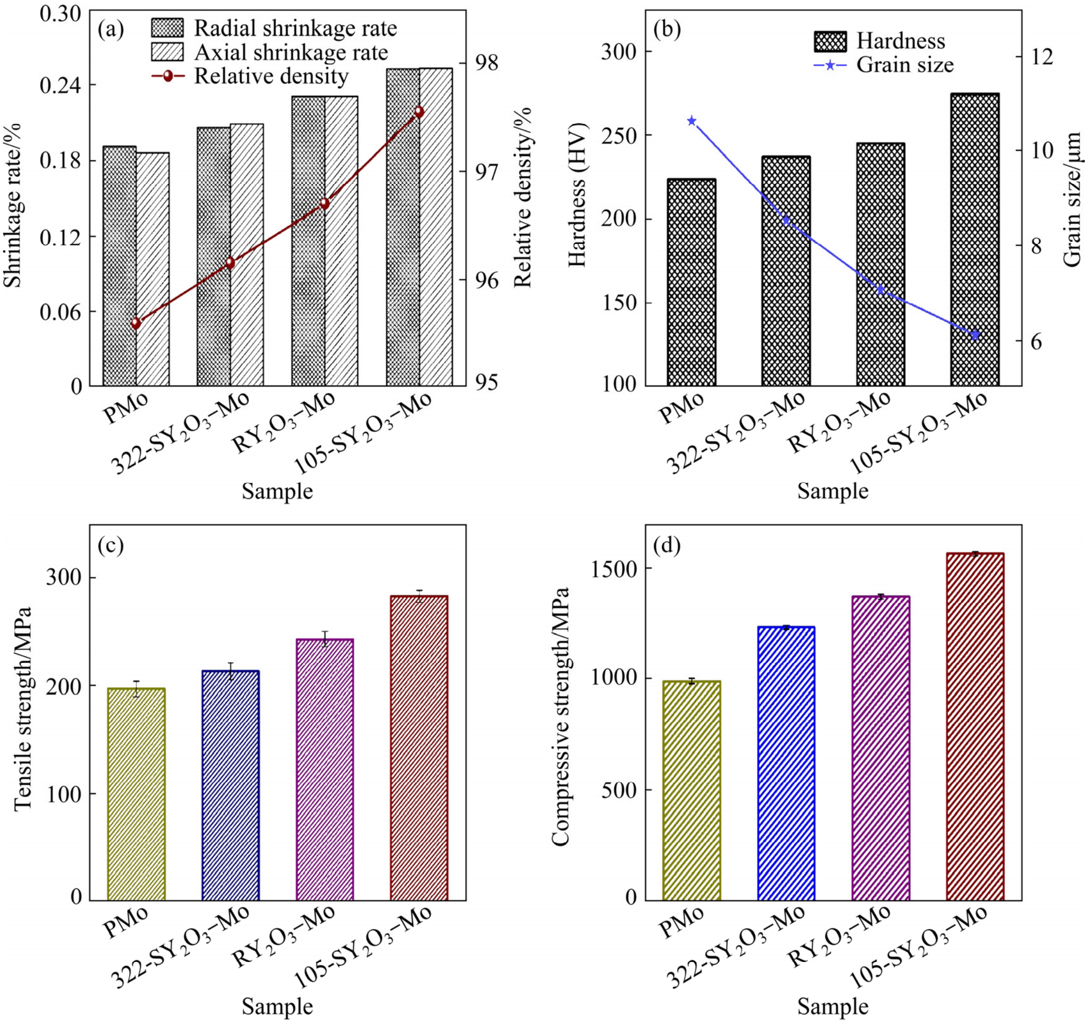

Fig. 5 Properties of PMo and various Mo−Y_2O_3 alloys: (a) Shrinkage rate and relative density; (b) Grain size and hardness; (c) Tensile strength; (d) Compressive strength

addition of Y_2O_3, and the 105-SY_2O_3−Mo exhibits the largest value of HV 274.6, increasing about 22.6% than that of PMo (HV 224). Moreover, Figs. 5(c) and (d) display the tensile and compressive strengths, respectively. We can see that the 105-SY_2O_3−Mo presents the largest tensile strength of 283.6 MPa, much larger than that of PMo (197.2 MPa) with an increase of about 43.8%. However, the 322-SY_2O_3−Mo and RY_2O_3−Mo only exhibit tensile strengths of 213.6 and 243.6 MPa with smaller increase of 8.3% and 23.5%, respectively. Meanwhile, the compressive strength follows the same trend as the tensile strength, and the compressive strength of 105-SY_2O_3−Mo is also the highest (1563.0 MPa). Obviously, the addition of Y_2O_3 can significantly enhance the mechanical properties of PMo, and the corresponding shape and size also play a crucial role in the strengthening effect.

To clarify the possible fracture mechanism, the fracture morphology of various samples is also captured and shown in Fig. 6. For sintered PMo billets, the grains are relatively clean but coarse, and a large number of pores have vanished with fully grown sintering neck, forming partially closed pores, which indicates that the closed pore spheroidization and shrinking stage have been finished [21−23]. Evidently, the fracture mode of PMo is intergranular without any dimples. For various sintered Mo−Y_2O_3 billets, Y_2O_3 particles can be clearly seen in the intracrystalline and intercrystalline of Mo grains. Although the fracture mode remains intergranular, the fracture is no longer smooth, and there are a few dimples and a tendency of transgranular fracture [24,25].

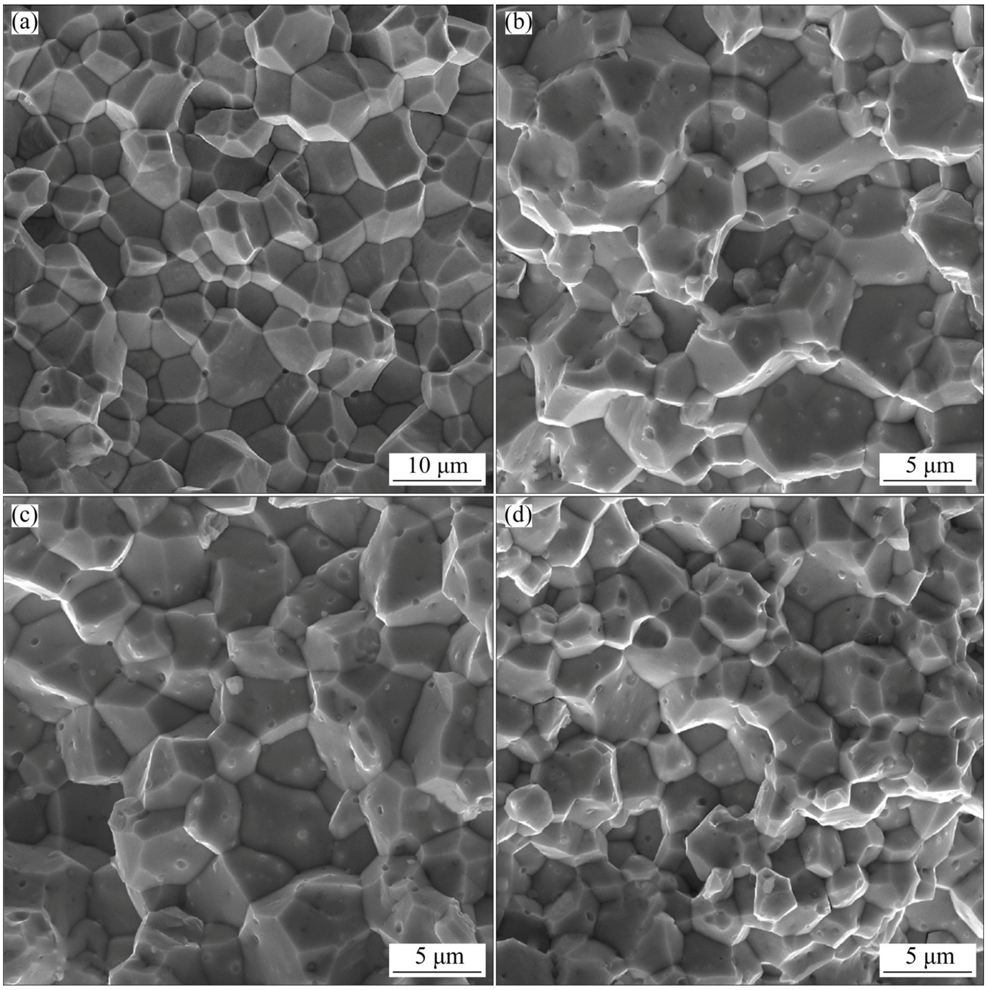

Fig. 6 Fracture morphologies of various samples: (a) PMo; (b) 322-SY_2O_3−Mo; (c) RY_2O_3−Mo; (d) 105-SY_2O_3−Mo

4 Discussion

The sintering procedure prompts the growth of sintering necks and crystals, the closing or vanishing of pores among particles, which is primarily mediated by surface, interface and volume diffusion [21−23]. All the atoms inside the grains take their own intrinsic position without damaging the chemical bond, but the outer surface of the grain is free and full of damaged chemical bonds, which determines the free surface energy. The greater the surface energy of crystal grains is, the larger the diffusivity is. When the second phase particles are minified, the corresponding surface area will increase and a higher breaking bond density and surface energy will be obtained [26]. A larger curvature radius can promote the sintering process, which means that when the second phase particles are smaller, larger curvature gradient and specific surface area can be obtained, as well as the broken bond density and surface energy, which would certainly accelerate the sintering procedure [3], as shown in the following equation [3,13]:

$$\sigma=\gamma k=\gamma\left(\frac{1}{R_1}+\frac{1}{R_2}\right)$$

where σ is the sintering driving force, γ is the surface energy of particles, k is the curvature, and R_1 and R_2 are the radii of the particles, respectively. In the interface diffusion procedure, the sintering driving force competes with extra surface energy resulting from submerging the second phase. Smaller particles mean lower extra surface energy and require only a shorter diffusion distance to swallow the second phase particles in the matrix [26,27]. Consequently, nano-scale second phase particles prefer to get inside the grains. To give direct evidence, TEM images of sintered billets are given in Fig. 7, and we can see that the second phase particles in 105-SY_2O_3−Mo are primarily intragranular (Figs. 7(a) and (b)), whereas Y_2O_3 particles in the 322-SY_2O_3−Mo alloy are mainly located at the grain boundaries, as revealed in Fig. 7(c). To provide a clear comparison, the distribution statistic results of second phase particles are obtained from the TEM images, as shown in Fig. 8. And we can infer that the critical particle size of the second phase is around 200 nm, and second phase particles with larger size prefer the intergranular distribution.

Intragranular second phase particles could interact with dislocations before the intergranular ones, increasing the resistance of dislocation migration to form dislocation loops (Fig. 7(a)) or change moving direction (Fig. 7(b)), which can cause dislocation pinning to prevent the dislocations from strong sliding field, accumulate and form microcracks at GBs. More importantly, because of the effective adsorption of Y_2O_3 on impurities [10], the second phase particles can significantly reduce impurity segregation at GBs, thereby improving the GB binding force. As a result, the strengthening effect of 105-SY_2O_3−Mo is superior to that of 322-SY_2O_3−Mo due to smaller particle size of second phase (Fig. 5). While, coarser second phase particles and diffused GBs create greater force during the interface diffusion process, causing second phase particles to move with the GBs together and eventually meet at the interfaces. However, because of the weak bonding force of GBs and the accumulation of dislocations, the second phase located at GBs is more likely to produce microcracks in the strong slip field [2,5,6], which is also revealed in Fig. 7(c).

Considering the fact that the particle size of 105-SY_2O_3 is close to that of RY_2O_3−Mo (around 100 nm), it is possible to directly compare and discuss their shape effects on the performances of Mo−Y_2O_3 alloys by ignoring the slight difference in the particle size. When spherical Y_2O_3 particles interact with dislocations, dislocation loops (Fig. 7(a)) exist around them or bypass the second phase by changing the expansion direction (Fig. 7(b)). The interaction between the particles and dislocations behaves similarly to that of spherical Y_2O_3 when the Y_2O_3 nanorods have relatively small aspect ratio. However, Y_2O_3 particles with larger aspect ratio (Fig. 7(d)) are easily cut or broken because of their sharp edges and corners, and the dislocations pass through them under shear stress, and continue to slip without changing direction [20]. When Y_2O_3 particles interact with stacking faults, they are more prone to produce stress concentration and microcracks.

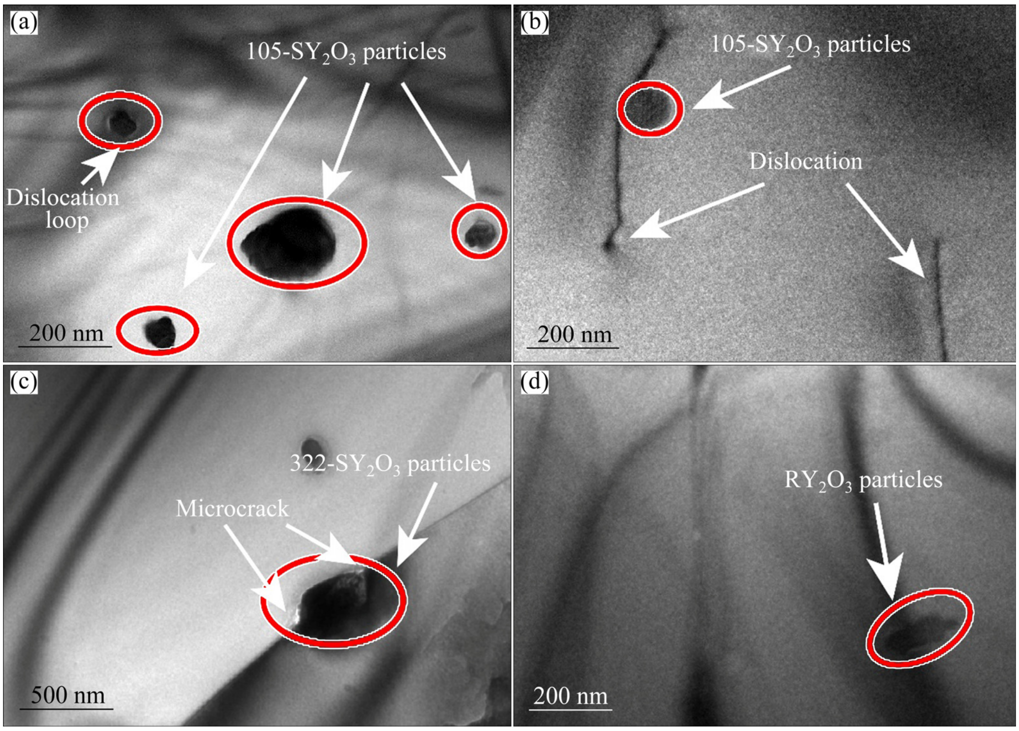

Fig. 7 TEM images of 105-SY_2O_3−Mo (a, b), 322-SY_2O_3−Mo (c), and RY_2O_3−Mo (d)

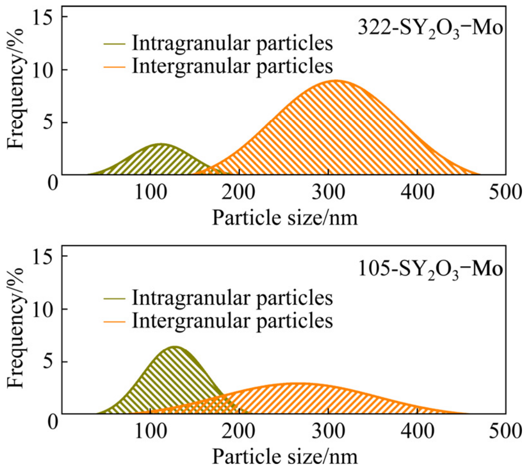

Fig. 8 Particle size distributions of second phases in 322-SY$_2$O$_3$–Mo and 105-SY$_2$O$_3$–Mo

5 Conclusions

(1) The shape and size of Y_2O_3 particles can be successfully controlled, and spherical particles with an average diameter of 105 nm have preferred strengthening effect.

(2) Smaller particle size of the second phase results in dominant intragranular distribution, and the critical size is about 200 nm.

(3) The shape and particle size of second phase play an important role in the determination of mechanical properties, and the latter is more important.

(4) The 105-SY$_2$O$_3$−Mo alloy exhibits the largest tensile strength which is enhanced by about 51.5% compared with that of pure Mo, much higher than that of 322-SY$_2$O$_3$−Mo (8.3%). Meanwhile, with similar second phase particle size (around 100 nm), the spherical shape leads to better strengthening effect than the rod-like one (RY$_2$O$_3$−Mo, 23.5%).

(5) The nanostructuring strategy of second phase could remarkably increase the tensile strength because of more intragranular distribution, which is highly effective and can be adopted in other dispersion reinforcing alloys.

Acknowledgments

This work was financially supported by the National Key R&D Program of China (No. 2017YFB0306001), and Guangxi Key Laboratory of Manufacturing System and Advanced Manufacturing Technology, China (No. 20-065-40-001k).

References

[1] WANG De-zhi, JI Yao-xin, WU Zhuang-zhi. Effects of cross rolling on texture, mechanical properties and anisotropy of pure Mo plates [J]. Transactions of Nonferrous Metals Society of China, 2020, 30: 2170−2176.

[2] WANG Lin, SUN Jun, LIU Gang, SUN Yuan-jun, ZHANG Guo-jun. Influences of annealing temperature on microstructure and mechanical properties of Mo−La$_2$O$_3$ [J]. International Journal of Refractory Metals and Hard Materials, 2011, 29: 522−527.

[3] LIU Guang-ren, ZHANG Guo-jun, JIANG Fu-jian, DING Xiang-dong, SUN Yuan-jun, SUN Jun, MA En. Nanostructured high-strength molybdenum alloys with unprecedented tensile ductility [J]. Nature Materials, 2013, 12: 344−350.

[4] CHENG Peng-ming, LI Shao-long, ZHANG Guo-jun, ZHANG Jin-yu, LIU Gang, SUN Jian-zhong. Ductilizing Mo−La$_2$O$_3$ alloys with ZrB$_2$ addition [J]. Materials Science and Engineering A, 2014, 619: 345−353.

[5] ZHANG Xiao, BU Chun-yang, WU Zhou, ZHUANG Fei. Effect of ZrO$_2$ addition on microstructure and properties of molybdenum [J]. China Molybdenum Industry, 2017, 41: 46−48. (in Chinese)

[6] REN Lei, ZHANG Yun-peng, ZHOU Hang. Preparation of Al$_2$O$_3$ reinforced molybdenum matrix composites and study on its properties [J]. Foundry Technology, 2013, 34: 547−549. (in Chinese)

[7] DAI Bao-zhu, WEI Shi-zhong, XU Liu-jie, PENG Guang-hui, LI Ji-wen, ZHANG Guo-shang. Effect of Al$_2$O$_3$ on structure and properties of molybdenum alloys [J]. Journal of Henan University of Science and Technology (Natural Science), 2010, 31: 1−4, 114. (in Chinese)

[8] ZHANG Jiu-xing, LIU Yan-qin, LIU Dan-min, ZHOU Mei-ling, ZUO Tie-yong. Toughness of La$_2$O$_3$-doped Mo alloy [J]. The Chinese Journal of Nonferrous Metals, 2004, 14: 13−17. (in Chinese)

[9] WU Zhuang-zhi, LIU Xin, WANG De-zhi. Synthesis of high-performance Mo−La$_2$O$_3$ powder by hydrogen reduction of MoO$_2$ originated from a self-reduction strategy [J]. Materials Research Express, 2019, 6: 126586.

[10] OLDS L E, RENGSTORFF G W P. Effects of oxygen, nitrogen, and carbon on the ductility of cast molybdenum [J]. JOM, 1956, 8: 150−155.

[11] HU Wei-qiang, SUN Tao, LIU Chen-xi, YU Li-ming, AHAMAD T, MA Zong-qing. Refined microstructure and enhanced mechanical properties in Mo−Y$_2$O$_3$ alloys prepared by freeze-drying method and subsequent low temperature sintering [J]. Journal of Materials Science & Technology, 2021, 88: 36−44.

[12] ZHANG Guo-jun, SUN Yuan-jun, ZUO Chao, WEI Jian-feng, SUN Jun. Microstructure and mechanical properties of multi-components rare earth oxide-doped molybdenum alloys [J]. Materials Science and Engineering A, 2008, 483/484: 350−352.

[13] SUN Guo-dong, ZHANG Guo-hua, CHOU Kuo-chih. Nanostructured oxide dispersion strengthened Mo alloys

from Mo nanopowder doping with oxide nanoparticles [J]. Journal of Materials Research and Technology, 2019, 8: 5753−5762.

[14] CHENG Peng-ming, ZHANG Guo-jun, ZHANG Jin-yu, LIU Gang, SUN Jun. Coupling effect of intergranular and intragranular particles on ductile fracture of Mo−La_2O_3 alloys [J]. Materials Science and Engineering A, 2015, 640: 320−329.

[15] LENCHUK O, ROHRER J, ALBE K. Atomistic modelling of zirconium and silicon segregation at twist and tilt grain boundaries in molybdenum [J]. Journal of Materials Science, 2016, 51: 1873−1881.

[16] YAO Li-ying, WEI Shi-zhong, ZHOU Yu-cheng, XU Liu-jie, CHEN Chong, SUN Tie-long, SHI Peng-peng. Preparation and characterization of Mo/ZrO_2−Y_2O_3 composites [J]. International Journal of Refractory Metals and Hard Materials, 2018, 75: 202−210.

[17] GUO Sheng-da, BAO Rui, YANG Jian-gao, CHEN Hao, YI Jian-hong. Effect of Mo and Y_2O_3 additions on the microstructure and properties of fine WC−Co cemented carbides fabricated by spark plasma sintering [J]. International Journal of Refractory Metals and Hard Materials, 2017, 69: 1−10.

[18] YAO Li-ying, GAO Yi-min, HUANG Yi-jie, LI Ye-fei, HUANG Xiao-yu, XIAO Peng. Fabrication of Mo−Y_2O_3 alloys using hydrothermal synthesis and spark plasma sintering [J]. International Journal of Refractory Metals and Hard Materials, 2021, 98: 105558.

[19] WU S H, CHEN D H. Synthesis of high-concentration Cu nanoparticles in aqueous CTAB solutions [J]. Journal of Colloid and Interface Science, 2004, 273:165−169.

[20] WANG De-zhi, LU Yao, LIU Xin-li, DUAN Bo-hua, WU Zhuang-zhi. Boosted mechanical properties of sintered MoLa alloys with ultrafine-grains by the nanostructuring of secondary phase [J]. Materials Science and Engineering A, 2020, 798: 140270.

[21] SUN Guo-dong, ZHANG Gua-hua, CHOU Kuo-chih. An industrially feasible pathway for preparation of Mo nanopowder and its sintering behavior [J]. International Journal of Refractory Metals and Hard Materials, 2019, 84: 105039.

[22] HASSOLD G N, CHEN I W, SROLOVITZ D J. Computer simulation of final-stage sintering: I. Model kinetics, and microstructure [J]. Journal of the American Ceramic Society, 1990, 73: 2857−2864.

[23] BLAINE D C, GUROSIK J D, PARK S J, GERMAN R M, HEANEY D F. Master sintering curve concepts as applied to the sintering of molybdenum [J]. Metallurgical and Materials Transactions A, 2006, 37: 715−720.

[24] KUMAR A, EYRE B L. Grain boundary segregation and intergranular fracture in molybdenum [J]. Proceedings of the Royal Society A, 1980, 370: 431−458.

[25] COCKERAM B V. The mechanical properties and fracture mechanisms of wrought low carbon arc cast (LCAC), molybdenum−0.5pct titanium−0.1pct zirconium (TZM), and oxide dispersion strengthened (ODS) molybdenum flat products [J]. Materials Science and Engineering A, 2006, 418: 120−136.

[26] FANG Zhi-gang, WANG Hong-tao, KUMAR V. Coarsening, densification, and grain growth during sintering of nano-sized powders—A perspective [J]. International Journal of Refractory Metals and Hard Materials, 2017, 62: 110−117.

[27] FANG Zhi-gang. Sintering of advanced materials [M]. Woodhead: Elsevier, 2010.

第二相形状和尺寸对烧结 Mo−Y_2O_3 合金力学性能的影响

吴壮志 [1,2]，赵 娜 [1]，卢 瑶 [1]，刘海浪 [3]，段柏华 [1,2]，刘新利 [1,2]，王德志 [1,2]

1. 中南大学 材料科学与工程学院，长沙 410083；
2. 中南大学 有色金属材料科学与工程教育部重点实验室，长沙 410083；
3. 桂林电子科技大学 广西制造系统与先进制造技术重点实验室，桂林 541004

摘　要：第二相的形貌和尺寸对氧化弥散强化钼合金的强化效果有很大影响。采用一种新策略来调节第二相 Y_2O_3 颗粒，研究颗粒形状和尺寸对烧结 Mo−Y_2O_3 合金力学性能的影响。结果表明，由于集中分布在晶粒内部第二相颗粒的钉扎位错，粒径小于 200 nm 的球形颗粒的强化效果最佳。添加粒径为 105 nm 球形 Y_2O_3 颗粒的钼合金抗拉强度提高约 43.8%，抗拉强度提高幅度远高于粒径为 322 nm 的第二相纳米球强化的钼合金(8.3%)。同时，在粒径相近(约 100 nm)的情况下，球状比一维棒状第二相的强化效果更好。

关键词：钼基合金；第二相；氧化钇；力学性能；弥散强化

(Edited by Wei-ping CHEN)